



Wall turbulence with designer properties

Beverley McKeon
CALIFORNIA INSTITUTE OF TECHNOLOGY

02/26/2016
Final Report

DISTRIBUTION A: Distribution approved for public release.

Air Force Research Laboratory
AF Office Of Scientific Research (AFOSR)/ RTB1
Arlington, Virginia 22203
Air Force Materiel Command

REPORT DOCUMENTATION PAGE					Form Approved OMB No. 0704-0188	
<p>The public reporting burden for this collection of information is estimated to average 1 hour per response, including the time for reviewing instructions, searching existing data sources, gathering and maintaining the data needed, and completing and reviewing the collection of information. Send comments regarding this burden estimate or any other aspect of this collection of information, including suggestions for reducing the burden, to the Department of Defense, Executive Service Directorate (0704-0188). Respondents should be aware that notwithstanding any other provision of law, no person shall be subject to any penalty for failing to comply with a collection of information if it does not display a currently valid OMB control number.</p>						
PLEASE DO NOT RETURN YOUR FORM TO THE ABOVE ORGANIZATION.						
1. REPORT DATE (DD-MM-YYYY) 02-09-2016		2. REPORT TYPE FINAL		3. DATES COVERED (From - To) November 2012 to November 2015		
4. TITLE AND SUBTITLE Wall turbulence with designer properties: Identification, characterization & manipulation of energy pathways			5a. CONTRACT NUMBER			
			5b. GRANT NUMBER FA-9550-12-1-0469			
			5c. PROGRAM ELEMENT NUMBER			
6. AUTHOR(S) McKeon, Beverley J.; Tropp, J. (California Institute of Technology) Goldstein, D. (University of Texas) Sheplak, M. (University of Florida)			5d. PROJECT NUMBER			
			5e. TASK NUMBER			
			5f. WORK UNIT NUMBER			
7. PERFORMING ORGANIZATION NAME(S) AND ADDRESS(ES) California Institute of Technology, Office of Sponsored Research 1200 E California Blvd Pasadena, CA 91125				8. PERFORMING ORGANIZATION REPORT NUMBER		
9. SPONSORING/MONITORING AGENCY NAME(S) AND ADDRESS(ES) Air Force Office of Science and Research 875 Randolph Street Room 3112 Arlington, VA 22203				10. SPONSOR/MONITOR'S ACRONYM(S) AFOSR		
				11. SPONSOR/MONITOR'S REPORT NUMBER(S)		
12. DISTRIBUTION/AVAILABILITY STATEMENT Approved for public release; distribution unlimited						
13. SUPPLEMENTARY NOTES						
14. ABSTRACT The research performed under this BRI award targeted the identification, characterization and manipulation of energy pathways in wall turbulence. The objectives were pursued separately and collaboratively by the California Institute of Technology (Caltech), the University of Florida (UF) and the University of Texas at Austin (UT) teams through a joint numerical, experimental and modeling effort. Our approach applied the team's state-of-the-art capabilities in experiments (Caltech), simulation (UT), MEMS sensor development (UF) and linear algebra techniques (Caltech) to the resolvent formulation of the Navier-Stokes equations for wall turbulence proposed by McKeon & Sharma (2010). This formulation explicitly identifies the pathways for extraction of energy from the mean flow and transfer between wavenumbers, and thus can be used to identify forcing distributions required to manipulate the spectrum. Energetic pathways between modes have been identified, highlighted and characterized by experimentally exciting two modes and providing the first-known observation of a single triadic interaction.						
15. SUBJECT TERMS Wall turbulence, energy transfer pathways, wall shear stress measurement, synthetic turbulence						
16. SECURITY CLASSIFICATION OF: a. REPORT b. ABSTRACT c. THIS PAGE		17. LIMITATION OF ABSTRACT	18. NUMBER OF PAGES 30	19a. NAME OF RESPONSIBLE PERSON Lisa Miller 19b. TELEPHONE NUMBER (Include area code) 626-395-3339		

INSTRUCTIONS FOR COMPLETING SF 298

- 1. REPORT DATE.** Full publication date, including day, month, if available. Must cite at least the year and be Year 2000 compliant, e.g. 30-06-1998; xx-06-1998; xx-xx-1998.
- 2. REPORT TYPE.** State the type of report, such as final, technical, interim, memorandum, master's thesis, progress, quarterly, research, special, group study, etc.
- 3. DATES COVERED.** Indicate the time during which the work was performed and the report was written, e.g., Jun 1997 - Jun 1998; 1-10 Jun 1996; May - Nov 1998; Nov 1998.
- 4. TITLE.** Enter title and subtitle with volume number and part number, if applicable. On classified documents, enter the title classification in parentheses.
- 5a. CONTRACT NUMBER.** Enter all contract numbers as they appear in the report, e.g. F33615-86-C-5169.
- 5b. GRANT NUMBER.** Enter all grant numbers as they appear in the report, e.g. AFOSR-82-1234.
- 5c. PROGRAM ELEMENT NUMBER.** Enter all program element numbers as they appear in the report, e.g. 61101A.
- 5d. PROJECT NUMBER.** Enter all project numbers as they appear in the report, e.g. 1F665702D1257; ILIR.
- 5e. TASK NUMBER.** Enter all task numbers as they appear in the report, e.g. 05; RF0330201; T4112.
- 5f. WORK UNIT NUMBER.** Enter all work unit numbers as they appear in the report, e.g. 001; AFAPL30480105.
- 6. AUTHOR(S).** Enter name(s) of person(s) responsible for writing the report, performing the research, or credited with the content of the report. The form of entry is the last name, first name, middle initial, and additional qualifiers separated by commas, e.g. Smith, Richard, J, Jr.
- 7. PERFORMING ORGANIZATION NAME(S) AND ADDRESS(ES).** Self-explanatory.
- 8. PERFORMING ORGANIZATION REPORT NUMBER.** Enter all unique alphanumeric report numbers assigned by the performing organization, e.g. BRL-1234; AFWL-TR-85-4017-Vol-21-PT-2.
- 9. SPONSORING/MONITORING AGENCY NAME(S) AND ADDRESS(ES).** Enter the name and address of the organization(s) financially responsible for and monitoring the work.
- 10. SPONSOR/MONITOR'S ACRONYM(S).** Enter, if available, e.g. BRL, ARDEC, NADC.
- 11. SPONSOR/MONITOR'S REPORT NUMBER(S).** Enter report number as assigned by the sponsoring/monitoring agency, if available, e.g. BRL-TR-829; -215.
- 12. DISTRIBUTION/AVAILABILITY STATEMENT.** Use agency-mandated availability statements to indicate the public availability or distribution limitations of the report. If additional limitations/ restrictions or special markings are indicated, follow agency authorization procedures, e.g. RD/FRD, PROPIN, ITAR, etc. Include copyright information.
- 13. SUPPLEMENTARY NOTES.** Enter information not included elsewhere such as: prepared in cooperation with; translation of; report supersedes; old edition number, etc.
- 14. ABSTRACT.** A brief (approximately 200 words) factual summary of the most significant information.
- 15. SUBJECT TERMS.** Key words or phrases identifying major concepts in the report.
- 16. SECURITY CLASSIFICATION.** Enter security classification in accordance with security classification regulations, e.g. U, C, S, etc. If this form contains classified information, stamp classification level on the top and bottom of this page.
- 17. LIMITATION OF ABSTRACT.** This block must be completed to assign a distribution limitation to the abstract. Enter UU (Unclassified Unlimited) or SAR (Same as Report). An entry in this block is necessary if the abstract is to be limited.

FINAL REPORT

Grant # FA-9550-12-01-0469

Wall turbulence with designer properties: Identification, characterization & manipulation of energy pathways

PI: Beverley McKeon
*Graduate Aerospace Laboratories
California Institute of Technology
Pasadena, CA 91125*

Joel Tropp
*California Institute of Technology
Pasadena, CA 91125*

Mark Sheplak
University of Florida

David Goldstein
University of Texas at Austin

Table of Contents

1. Introduction	3
1.1 Objectives	3
1.2 Dissemination of results	3
1.2.1 Archival journals	3
1.2.2 Conference papers	4
1.2.3 Conference presentations.....	4
1.3 Outline of report	6
2. Technical Background.....	7
3. Analytical Developments.....	9
3.1 Development of the resolvent analysis for wall turbulence	9
3.2 Mathematical tools and structure	10
3.3 Fundamental contributions to understanding of wall turbulence	10
3.4 Reconciliation of resolvent modes with turbulence simulation	11
4. Direct Numerical Simulations.....	13
4.1 Overview	13
4.2 Numerical method	13
4.3 Results	14
5. Capacitive Shear Stress Sensor Development	19
5.1 Sensor fabrication.....	19
5.2 Sensor packaging.....	20
5.3 Interface circuitry	21
5.4 Characterization	22
6. Experimental Results.....	25
6.1 Experimental set-up.....	25
6.2 Characterization of a single synthetic mode	26
6.3 Manipulation of energetic pathways	27
7. Summary, Conclusions and Outlook	29
References	30

1. Introduction

The research performed under this BRI award targeted the identification, characterization and manipulation of energy pathways in wall turbulence. Teams at the California Institute of Technology (Caltech), the University of Florida (UF) and the University of Texas at Austin (UT) contributed to the research and to this report.

1.1 Objectives

The specific objectives of this research, as identified in the original proposal, were as follows.

Manipulate the dominant energy pathways in the turbulent spectrum in incompressible wall turbulence by exploiting sensitivity to small wall perturbations.

1. **Identify and characterize the pathways in simulation and experiment** by over-stimulation of individual critical layer modes (akin to adding a tracer to individual pathways) and direct measurement of velocities and wall shear stress (using hot wire anemometry, particle image velocimetry and the UF shear stress sensor).
2. **Develop low-order mathematical representations of the dominant energy pathways** using state-of-the-art matrix approximation techniques.
3. **Demonstrate sustained “designer turbulence”**, in which a desirable turbulent spectrum and/or mean velocity profile (wall shear stress) are maintained using wall forcing created either using simple mechanical mechanisms or a (meta-)material wall with properties tailored to manipulate key energy pathways.

The objectives were pursued separately and collaboratively by the Caltech, UF and UT teams through a joint numerical, experimental and modeling effort. Our approach applied the team's state-of-the-art capabilities in experiments (Caltech), simulation (UT), MEMS sensor development (UF) and linear algebra techniques (Caltech) to the resolvent formulation of the Navier-Stokes equations for wall turbulence proposed by McKeon & Sharma (2010), which is outlined in brief in section 2. This formulation explicitly identifies the pathways for extraction of energy from the mean flow and transfer between wavenumbers, and thus can be used to identify forcing distributions required to manipulate the spectrum.

1.2 Dissemination of results

1.2.1 Archival journals

1. Moarref, R., Sharma, A. S., Tropp, J. A. & McKeon, B. J. ‘Model-based scaling and prediction of the streamwise energy intensity in high-Reynolds number turbulent channels’ *J. Fluid Mech.* 734, 275-316; *also ArXiV1302.1594*, 2013.
2. Luhar, M., Sharma, A. S. & McKeon, B. J. ‘On the structure and origin of pressure fluctuations in wall turbulence: predictions based on the resolvent analysis’ *J. Fluid Mech.*, 751, 38-70 (2014).
3. Luhar, M., Sharma, A. S. & McKeon, B. J. ‘Opposition control within the resolvent analysis framework’ *J. Fluid Mech.*, 749, 597-626 (2014).

4. Moarref, R., Jovanovic, M. R., Tropp, J. A., Sharma, A. S. & McKeon, B. J. 'A low-order decomposition of turbulent channel flow via resolvent analysis and convex optimization' *Phys. Fluids*, 26, 051701 (2014); also *ArXiV* 1401.6417, 2014.
5. Duvvuri, S. & McKeon, B. J. 'Triadic scale interactions in a turbulent boundary layer' *J. Fluid Mech.*, 767, R4 (2015).
6. Luhar, M., Sharma, A. S. & McKeon, B. J. 'A framework for studying the effect of compliant surfaces on wall turbulence' *J. Fluid Mech.*, 768, 415-441 (2015); also *arXiv* 1411.6690.
7. Sharma, A. S., Moarref, R., McKeon, B. J., Park, J. S., Graham, M. & Willis, A. P. 'Low-dimensional representations of exact coherent states of the Navier-Stokes equations' (*To appear, Phys. Rev. E.*)

Under review:

Luhar, M., Sharma, A. S. & McKeon, B. J. 'On the design of optimal compliant walls for turbulence control'.

There are several additional manuscripts in preparation arising from work under this grant.

1.2.2 Conference papers

1. Moarref, R., Park, J.-S., Sharma, A. S., Willis, A. P., Graham, M. D. & McKeon, B. J. 'Approximation of the exact traveling wave solutions in wall-bounded flows using resolvent modes' *TSFP-9, Melbourne (Turbulent Shear Flow Phenomena Symposium -9)*, July 2015.
2. Luhar, M., Sharma, A. S. & McKeon, B. J. 'On the design of optimal compliant walls for turbulence control' *TSFP-9, Melbourne (Turbulent Shear Flow Phenomena Symposium -9)*, July 2015.
3. Duvvuri, S. & McKeon, B. J. 'Skewness and amplitude modulation coefficient as measures of phase in triadic scale interactions' *TSFP-9, Melbourne (Turbulent Shear Flow Phenomena Symposium -9)*, July 2015.
4. Gómez Carrasco, F., Blackburn, H., Rudman, M., Sharma, A. S. & McKeon, B. J. 'Driving very large-scale motions in turbulent pipe flow' *TSFP-9, Melbourne (Turbulent Shear Flow Phenomena Symposium -9)*, July 2015.

1.2.3 Conference presentations

- You, S. and Goldstein, D., 'The effect of spatial discretization upon traveling wave body forcing of a turbulent wall-bounded flow', *Paper R21.00007, 68th Meeting of the American Physical Society Division of Fluid Dynamics, Boston, MA, Nov., 2015*.
- Beverley McKeon, 'The relationship between amplitude modulation, coherent structure and critical layers in wall turbulence', *Paper E19.00001, 68th Meeting of the American Physical Society Division of Fluid Dynamics, Boston, MA, Nov., 2015*.
- Subrahmanyam Duvvuri & Beverley McKeon, 'Non-linear scale interactions in a forced turbulent boundary layer', *Paper H22.00003, 68th Meeting of the American Physical Society Division of Fluid Dynamics, Boston, MA, Nov., 2015*.
- Duvvuri, Subrahmanyam and McKeon, Beverley J. (2014) 'Phase relationships in presence of a synthetic large-scale in a turbulent boundary layer' In: 44th AIAA Fluid Dynamics Conference, 16-20 June 2014, Atlanta, GA.

- A. Sharma, R. Moarref, M. Luhar, D. B. Goldstein, B. J McKeon (2014) ‘*Effects of a gain-based optimal forcing on turbulent channel flow*’ In: Aerospace Sciences Meeting, National Harbor, MD, AIAA-2014-1450, 2014.
- Beverley McKeon, Michael Graham, Rashad Moarref, Jae Sung Park, Ati Sharma & Ashley Willis, ‘*Approximation of traveling wave solutions in wall-bounded flows using resolvent modes*’, *Paper A26.00005, 67th Meeting of the American Physical Society Division of Fluid Dynamics, San Francisco, CA, Nov., 2014.*
- Kevin Rosenberg & Beverley McKeon, ‘*Resolvent mode identification in a turbulent boundary layer*’, *Poster F1.00035, 67th Meeting of the American Physical Society Division of Fluid Dynamics, San Francisco, CA, Nov., 2014.*
- Rashad Moarref, Ati Sharma, Joel Tropp & Beverley McKeon, ‘*Nonlinear interactions and their scaling in the logarithmic region of turbulent channels*’, *Paper A18.00002, 67th Meeting of the American Physical Society Division of Fluid Dynamics, San Francisco, CA, Nov., 2014.*
- Subrahmanyam Duvvuri & Beverley McKeon, ‘*Phase relations of triadic scale interactions in turbulent flows*’, *Paper A26.00005, 67th Meeting of the American Physical Society Division of Fluid Dynamics, San Francisco, CA, Nov., 2014.*
- Mitul Luhar, Ati Sharma & Beverley McKeon, ‘*A framework for studying the effect of compliant surfaces on wall turbulence*’, *Paper A20.00008, 67th Meeting of the American Physical Society Division of Fluid Dynamics, San Francisco, CA, Nov., 2014.*
- Jae Sung Park, Rashad Moarref, Beverley McKeon, Michael Graham, ‘*A comprehensive investigation of exact coherent states in Newtonian channel flow*’, *Paper A17.00001, 67th Meeting of the American Physical Society Division of Fluid Dynamics, San Francisco, CA, Nov., 2014.*
- S. Duvvuri, M. Luhar, C. Barnard, M. Sheplak, B. McKeon ‘*A study of synthetic large scales in turbulent boundary layers*’ *66th Meeting of the American Physical Society Division of Fluid Dynamics, Pittsburgh, PA, Nov., 2013.*
- M. Luhar, A. S. Sharma & B. J. McKeon, ‘*Deconstructing the effectiveness of opposition control in turbulent pipe flow*’ *66th Meeting of the American Physical Society Division of Fluid Dynamics, Pittsburgh, PA, Nov., 2013.*
- B. J. McKeon & D. Chung ‘*Phase relationships and amplitude modulation in wall turbulence*’ *66th Meeting of the American Physical Society Division of Fluid Dynamics, Pittsburgh, PA, Nov., 2013.*
- C. Barnard, J. Meloy, M. Sheplak ‘*Development of a MEMS shear stress sensor for use in wind tunnel applications*’ *66th Meeting of the American Physical Society Division of Fluid Dynamics, Pittsburgh, PA, Nov., 2013.*
- A. Sharma & B. McKeon ‘*Nonlinearity and the energy cascade in the resolvent analysis of wall turbulence*’ *66th Meeting of the American Physical Society Division of Fluid Dynamics, Pittsburgh, PA, Nov., 2013.*
- A. Sharma, R. Moarref, M. Luhar, D. Goldstein & B. McKeon ‘*An investigation of the flow modification in a turbulent channel with gain-based optimal forcing*’ *66th Meeting of the American Physical Society Division of Fluid Dynamics, Pittsburgh, PA, Nov., 2013.*
- B. J. McKeon, D. Chung & I. Jacobi ‘*On phase relationships in wall turbulence*’ *Symposium for Fazle Hussain, Puerto Rico, Nov. 2013.*
- McKeon, B. J. ‘*INVITED: Perspectives on wall-bounded turbulent flows*’ *AIAA-2013.*

1.3 Outline of report

After a brief technical introduction in section 2, we outline the analytical and modeling developments made under this grant (section 3), the results of the DNS study using idealized body forces to artificially perturb an otherwise canonical turbulent channel flow (section 4), the development of a miniature capacitive shear stress sensor capable of characterizing the shear stress associated with perturbed wall turbulence (section 5), and experiments towards deterministic perturbation of a turbulent boundary layer (section 6). A summary and recommendations for future work are given in section 7. The work has been reported in detail in the publications listed above; the goal of the present report is the synthesis of the major contributions arising from this work.

2. Technical Background

The resolvent formulation for wall turbulence is a central part of much of the research performed under this grant. A brief background to the essential components of this analysis is given here.

It is increasingly clear that full identification of the energy pathways in turbulent flows requires a systems-level approach, in which the characteristics of the flow are considered at a global rather than local level. This type of analysis is standard in the transition community, in which stability can be explored by investigating the properties of the linearized Navier-Stokes operator (in either a linear stability or transient growth sense) or the full nonlinear equations.

McKeon & Sharma (2010) formulated the NSE for turbulent pipe flow as an input-output relationship for every streamwise/spanwise wavenumber and frequency, henceforth (k, n, ω) , of velocity fluctuations in turbulent pipe flow (effectively a decomposition into helical waves). The transfer functions, $H_{kn\omega}$, are linear (and thus require a priori knowledge of the mean velocity profile), but this is a complete representation of the NSE in which the nonlinear terms are explicitly retained and treated. Figure 2.1 shows a schematic of the NSE under this decomposition.

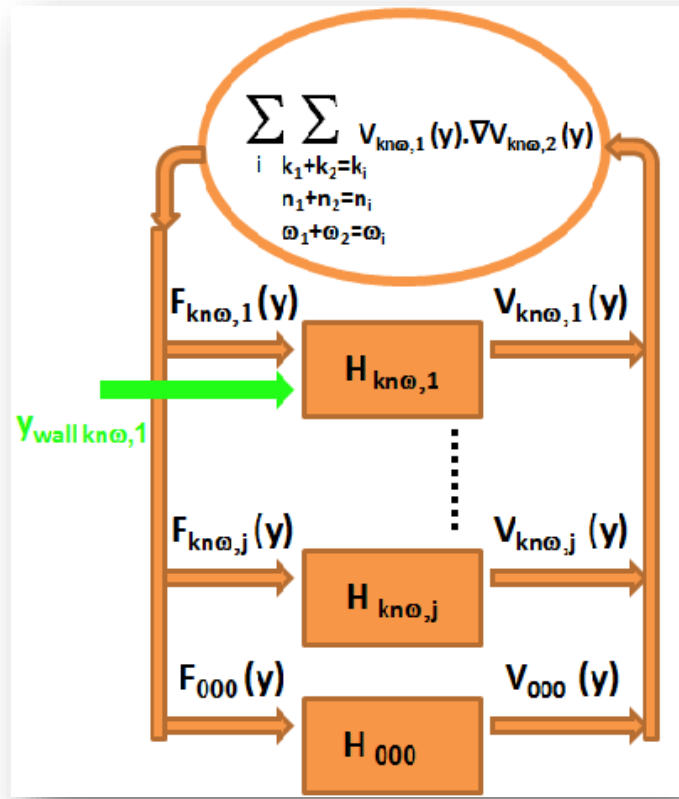


Figure 1: Schematic of the Navier-Stokes formulation of McKeon & Sharma, showing capability to consistently include excitation at the wall, y_{wall} .

A major contribution of this work was the analysis of the form of $H_{kn\omega}$ for (k,n,ω) combinations observed in real turbulence under unstructured forcing, equivalent to seeking the "most dangerous directions" of forcing which lead to the most amplified response. This led to the determination that these transfer functions could be considered to be low rank and therefore well approximated by the first modes calculated under a simple singular value decomposition. The implication, then, is that the first singular response mode is so highly amplified that it will dominate the velocity field at this (k,n,ω) , so long as a non-zero component of forcing in this "most dangerous direction" exists in the real flow (which is highly likely in a turbulent flow). This model has subsequently been shown to be capable of capturing key "building blocks" of wall turbulence, from spectral scaling results to the appearance of coherent structure such as hairpin vortex packets. The implications of the effectiveness of this low rank approximation are far-reaching in terms of understanding canonical flows and modeling perturbed cases, and have been explored in the present research. While the approach can be extended to more complex flows, the constrained parameter space and mathematical simplifications associated with canonical flows assist efforts to develop understanding and modeling tools.

Full information on the resolvent formulation can be obtained from prior literature (McKeon & Sharma, 2010; McKeon, Sharma & Jacobi, 2013; Sharma & McKeon, 2013) and from the papers arising from work funded under this grant, as listed in section 1.2.1.

3. Analytical Developments

3.1 Development of the resolvent analysis for wall turbulence

The resolvent formulation has been modified from enforcing the continuity equation via an explicit selection of a divergence-free basis for the analysis to one in which continuity is enforced directly, allowing the use of the analysis in controlled flows (for which a divergence-free basis cannot be calculated a priori).

This development allowed an extension of earlier investigations into which aspects of the velocity field of incompressible wall turbulence were correctly captured by resolvent analysis to consider pressure fluctuations. In particular, it was shown that many of the key relationships between the velocity field, coherent structure and high-amplitude wall pressure events observed in previous experiments and DNS were reconciled by simple summation of resolvent modes (see figure 3.1). in addition, the possibility of amplitude modulation of the pressure fluctuations in a manner similar to that observed in the velocity fluctuations was identified.

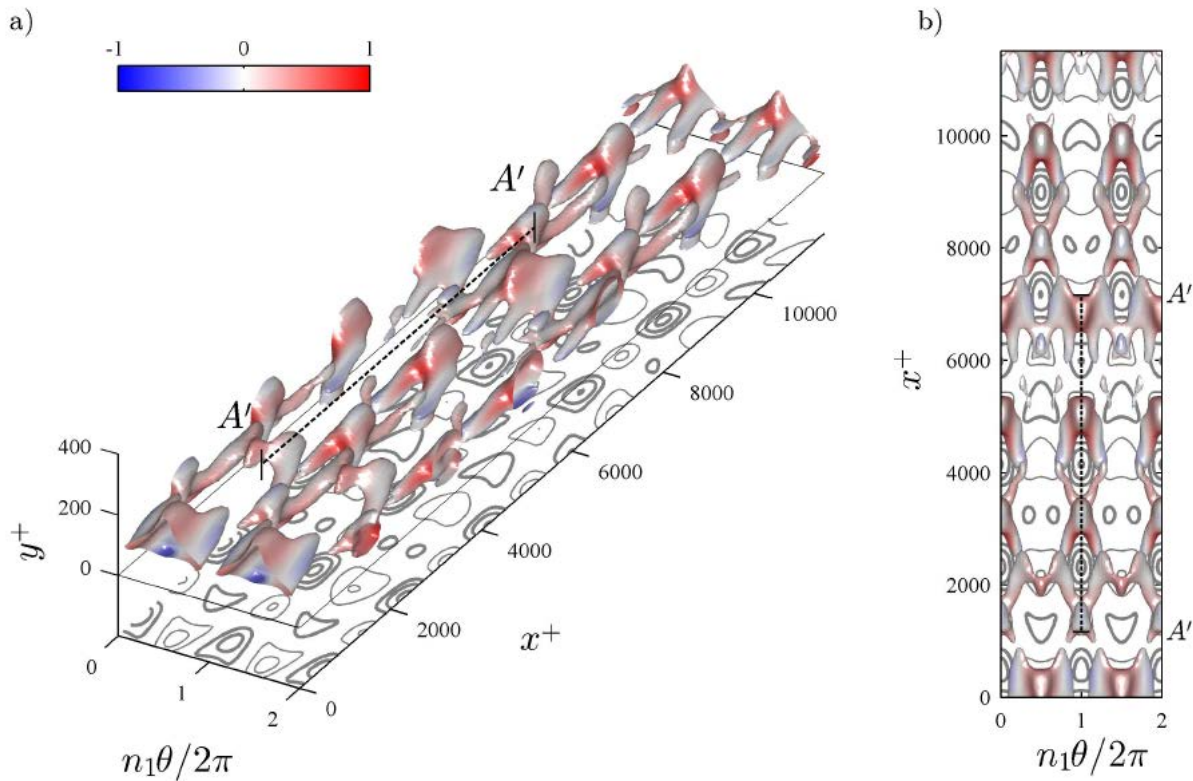


Figure 3.1. Isosurfaces of constant swirling strength (at 50% of maximum) for an assembly of three resolvent modes whose wavenumbers and frequencies sum to zero, i.e. are triadically-consistent. The isosurfaces are shaded based on the local azimuthal vorticity. Red denotes prograde rotation, i.e. with the sense of the mean vorticity, and blue denotes retrograde rotation. The contours beneath the isosurfaces represent the normalized wall pressure field. Bold contours show positive pressure, fine contours show negative pressure. (a) isometric view, (b) plan view.

By incorporating first opposition control (a linear wall boundary condition imposing a wall-normal velocity at the wall of opposite sign to the signal observed at a senior plane above the wall), and then a simple model of a coupled compliant wall, the ability of the resolvent analysis to capture the trends implied by full direct numerical simulation was demonstrated. The importance of the phase of opposition control to the overall drag reduction, which increases with increasing Reynolds numbers was outlined, and a means for ensuring that the strategy did not lead to drag increase for any of the range of controlled modes was identified. Similarly, the ability of a simple model of a compliant wall using a complex admittance function to model the relationship between wall-normal velocity and pressure captured both the first order change in amplification of modes already present in the turbulent spectrum as well as the increased amplification associated with two-dimensional modes. This is a likely explanation for observations of large-scale 2D traveling waves which negate the drag reduction found for compliant walls at low Reynolds number and/or in small domains (not shown here).

3.2 Mathematical tools and structure

All resolvent results shown in this report were produced using Matlab running on a standard laptop, i.e. significantly faster than DNS of wall turbulence at any reasonable Reynolds number, and fast enough to permit optimization and searching of parameter spaces as part of the analysis. The speed-up of this already fast analysis associated with the use of randomized matrix approximation in the singular value decomposition of the resolvent operator at the heart of this analysis was estimated to be of order 50%.

Our investigations have uncovered and explained the origin of sparsity in the frequency domain. Essentially, the presence of a critical layer where the local mean velocity is equal to the convection velocity of a wavelike perturbation localizes the region of high amplification around it. In a spatially-discretized system, then, energetic frequencies are limited to those that are determined by the product of the appropriate critical layer mean velocity and the streamwise wavenumber, such that frequencies outside of this localized region are not energetic.

At heart, the discoveries of mathematical structure associated with the resolvent formulation confirm the appropriateness of the approach for the treatment of wall turbulence. They emphasize that the spatial inhomogeneity (anisotropy) imposed by the presence of the wall both complicates understanding, for example because the Fourier basis is no longer the energetically correct basis for expansion in the wall-normal direction, but also provide simplification in terms of the description of possible mechanisms for energy transfer associated with the critical layer.

3.3 Fundamental contributions to the understanding of wall turbulence

We identified the scaling of the resolvent operator that translates to the velocity fluctuations through the scaling of the mean velocity profile in early work under this grant. That effort led to a tool for the approximation of the streamwise stress with increasing Reynolds number.

We have also identified connections between observations of amplitude modulation and skewness profiles in wall turbulence and the relative phase between modes that interact through the nonlinear convective term in the NSE via a triadically-consistent triplet of wavenumbers and frequencies.

Further, the equations governing the fluctuating stresses can be used to formulate a new transfer function relating velocity at one scale to the stress at the same scale arising from the interaction of two other modes. Analysis of this transfer function reveals that the critical layer controls the relative phases of these two signals, as shown in schematic in figure 4.2. This realization permits the use of a synthetically-excited external scale to modify scale interactions and energy transfer pathways in both experiments and simulation, as shown in the following sections.

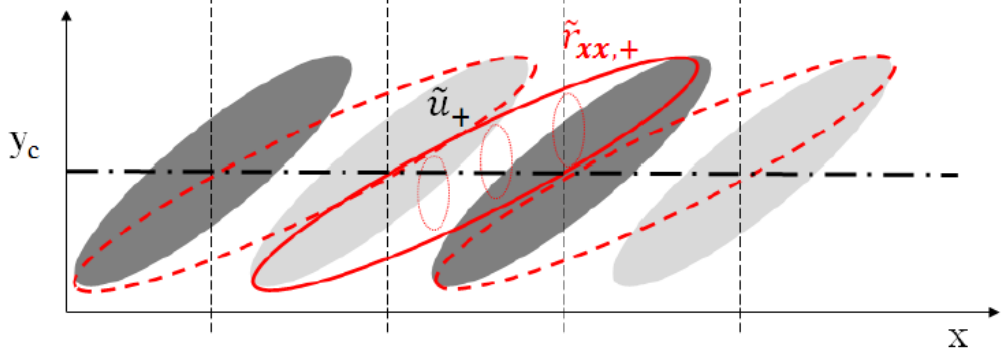


Figure 3.2. Cartoon of the relative physical positioning of the streamwise velocity associated with a single large-scale mode (u) and the streamwise stress at the same scale (r_{xx}), showing how the envelope of the stress leads the velocity by a quarter period at the critical layer, y_c , as observed in experiment and simulation.

3.4 Reconciliation of resolvent modes with turbulence simulations

Some results of the solution of a convex optimization problem designed to optimally represent DNS velocity spectra in terms of resolvent modes are shown in figure 3.2. With increasing numbers of singular response modes, the spectral match becomes increasingly good. While the wall-parallel components are well-captured, the disagreement arising in the wall-normal fluctuations is a subject of ongoing work.

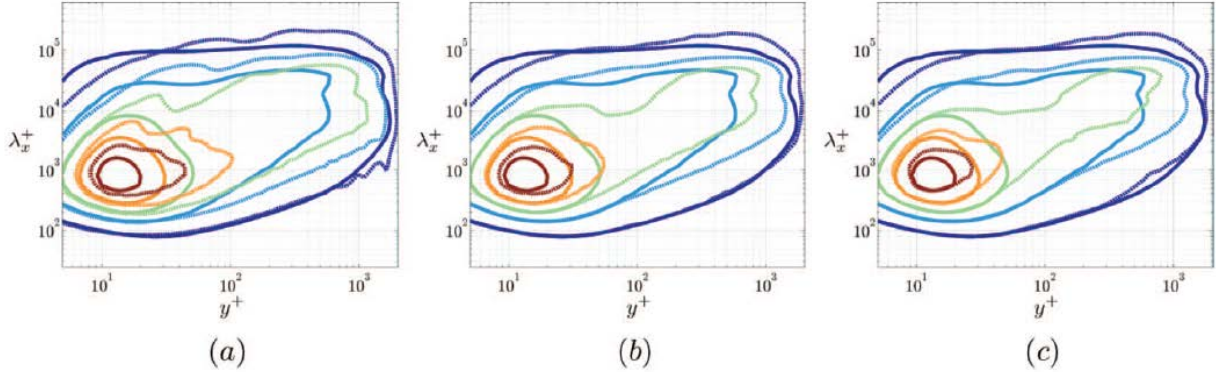


Figure 3.3. Comparison between the streamwise wavenumber spectra of the streamwise velocity obtained by DNS (solid lines) and from the optimal representation in terms of resolvent modes. Contours show 10% to 90% of the DNS maximum in increments of 20%. Left-to-right: increasing numbers of resolvent singular modes per wavenumber (2, 6 and 12 pairs, respectively).

Resolvent analysis also provides an efficient way to represent exact coherent state (ECS) traveling wave solutions of the NSE. The ECS are exact solutions of the NSE with certain imposed symmetries, and are understood to form an important part of the state space representation of wall

turbulence. As shown in figure 3.4, the resolvent mode projection of one ECS captures its behavior extremely well, from the instantaneous velocity field in the cross-stream, y - z plane, to the mean velocity profile regenerated from the captured Reynolds stress profile (not shown). The potential for unification of the resolvent and ECS views of wall turbulence, and for resolvent analysis to lead to a cheaper and more efficient way to find new ECS solutions is an exciting topic of ongoing work.

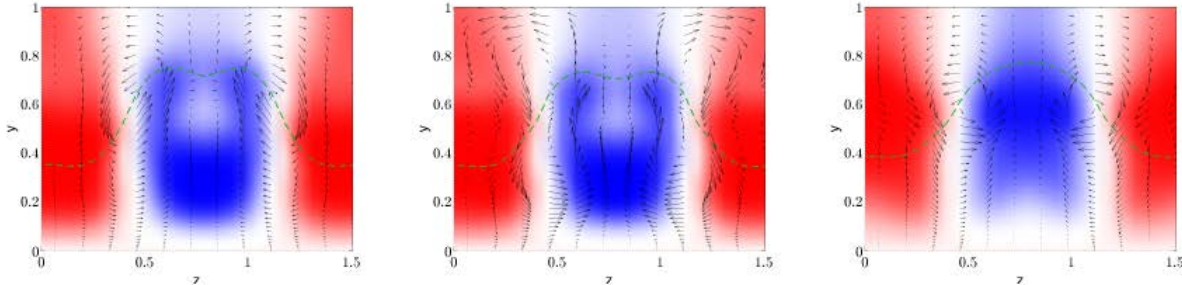


Figure 4.2. Comparison between exact coherent state solution P4 lower branch and the projection of the ECS onto resolvent modes in the cross-stream plane. Left-to-right: actual solution; projection onto 5 resolvent mode pairs per spatial Fourier mode (capturing 92% of the fluctuation energy); projection onto 1 resolvent mode pair per spatial Fourier mode.

4. Direct Numerical Simulations

The DNS study at the University of Texas examined the receptivity of a turbulent channel flow to two- and three-dimensional near-wall body forcing. A forced turbulent channel at $Re_\tau = 180$ with a constant mean pressure gradient was considered as representative of the near-wall physics of a zero pressure gradient turbulent boundary layer. The wave-like body forcing shape was obtained from the resolvent analysis of McKeon and Sharma (2010) for wave numbers and wave speeds characteristic of the near-wall turbulence sustainment cycle. The amplitude of the forcing function was varied as the velocity and kinetic energy obtained from the DNS were decomposed into a mean, a wave, and a turbulent component and the exchange of energy between those components was explored.

4.1 Overview

We begin this review with the fluid physics key findings: 3D forcing causes greater changes to the mean velocity profile than does 2D forcing of the same amplitude. The changes in the mean velocity profile are associated with changes in the Reynolds stress of the wave- and turbulent-components. For 2D forcing, the external power required to drive the response is the dominant term in the wave kinetic energy budget. For 3D forcing, the external power input is small compared to the power drawn from the mean flow suggesting that once perturbed, the 3D wave response is able to sustain itself by drawing energy from the mean. Enhanced spanwise mixing is caused by the presence of counter-rotating streamwise vortices in the case of 3D forcing and there is a coupling of the response mode and other parts of the turbulence spectrum that is even significant for small 3D forcing amplitudes. The magnitude of the velocity response scales with the square root of forcing amplitude, A , for large amplitudes and A itself for small amplitudes. If 2D forcing is applied via discrete regions of actuation rather than continuously in space, spanwise discretization may yield a coupling of the forcing to the flow that is nearly as strong as the continuous 3D forcing.

4.2 Numerical method

Direct numerical simulations of the Navier Stokes equations (Eqns. 1) were performed.

$$\frac{\partial u_j}{\partial x_j} = 0 \quad (1a)$$

$$\frac{\partial u_1}{\partial t} + \frac{\partial u_1 u_j}{\partial x_j} = -\frac{1}{\rho} \frac{\partial p}{\partial x_1} + \nu \frac{\partial^2 u_1}{\partial x_j \partial x_j} - A \cos(k_3 x_3) \Re \left\{ \hat{f}_1(x_2) \exp[i(k_1 x_1 - \omega t)] \right\} \quad (1b)$$

$$\frac{\partial u_2}{\partial t} + \frac{\partial u_2 u_j}{\partial x_j} = -\frac{1}{\rho} \frac{\partial p}{\partial x_2} + \nu \frac{\partial^2 u_2}{\partial x_j \partial x_j} - A \cos(k_3 x_3) \Re \left\{ \hat{f}_2(x_2) \exp[i(k_1 x_1 - \omega t)] \right\} \quad (1c)$$

$$\frac{\partial u_3}{\partial t} + \frac{\partial u_3 u_j}{\partial x_j} = -\frac{1}{\rho} \frac{\partial p}{\partial x_3} + \nu \frac{\partial^2 u_3}{\partial x_j \partial x_j} + A \sin(k_3 x_3) \Im \left\{ \hat{f}_3(x_2) \exp[i(k_1 x_1 - \omega t)] \right\} \quad (1d)$$

The subscripts j take values (1,2,3) to denote streamwise, wall-normal and spanwise directions, respectively. The forcing with real and imaginary parts has frequency ω , amplitude A and streamwise and spanwise wave numbers k_1 and k_3 . The chosen wave numbers and frequency (with phase velocity, $c^+ = c/u_\tau \approx 10$ where $c = \omega/k_1$) are representative of the energetic near-wall cycle. The external force field is applied in addition to the mean pressure gradient required to sustain the turbulent channel flow at $Re_\tau = 180$ in a channel spanned by a mesh of 128^3 grid points. The details of the development of the DNS code are given in previous publications (Goldstein et al, 1993, 1995) and the details of the turbulence statistics for the channel simply forced by a mean pressure

gradient were validated with the results of Kim (2011) and Moser et al, (1999). In order to understand the flow response to the introduced forcing waves, the velocity and pressure are divided into a mean, wave and turbulent component based on the phase-locked averaging technique of Reynolds and Hussain (1972). For example, $\mathbf{U}(\mathbf{x},t) = \bar{\mathbf{U}}(x_2) + \tilde{\mathbf{U}}(\mathbf{x},t) + \mathbf{U}''(\mathbf{x},t)$. The flow can then be described in terms of the turbulent Reynolds shear stress due to the passage of the wave and a second term describing the Reynolds shear stress just due to the wave itself. Moreover, the decomposition allows us to describe the exchange of energy between the mean flow, the wave response and the turbulent fluctuations.

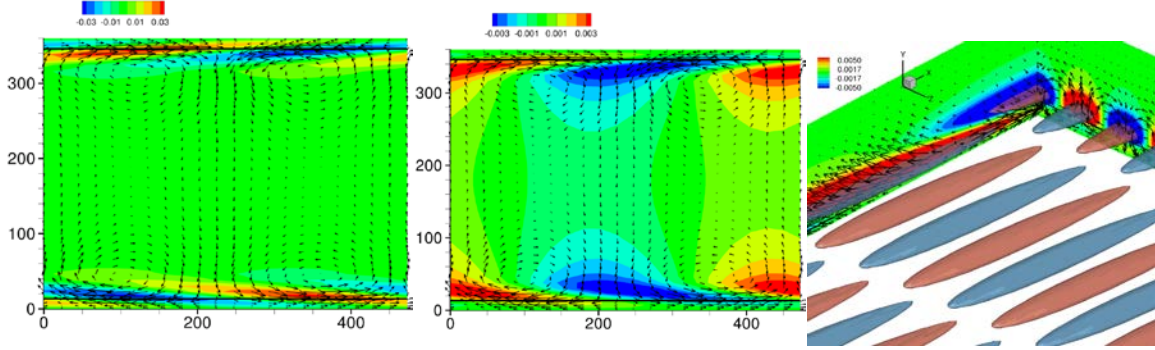


Figure 4.1. The streamwise (a) and wall-normal (b) shapes (in wall units, normalized by u_r^3/v) obtained from the resolvent analysis are shown for one particular 2D forcing case. The vector field associated with the velocity response is overlaid. The horizontal axis is the streamwise coordinate ($0 \leq x^+ \leq 480$) and the vertical axis is the wall-normal coordinate ($0 \leq y^+ \leq 360$). The location of the critical layer where $\bar{U}^+ = 10$ is shown as a solid black line. In (c) are isosurfaces of streamwise forcing (positive in red, negative in blue) and color contours of the wall-normal forcing (in wall units) obtained from the resolvent analysis are shown on XY and YZ planes for a 3D case. The vector fields in those two planes are also shown.

4.3 Results

The velocity response to the imposed forcing using the above phase averaging procedure and displayed as vectors atop the 2D forcing field in color contours in Fig. 4.1a,b or 3D force fields in Fig. 4.1c for one particular forcing level at one particular phase. The magnitude of the streamwise forcing is almost an order of magnitude greater than that of the wall-normal forcing. The wave-like nature of the forcing causes a weak mean sloshing of the fluid close to the wall. The magnitude of the peak phase averaged velocity response occurs close to the location of peak force magnitude and the maximum wall-normal response occurs about midway between the peaks in the streamwise components. In the 3D result one can see the presence of spanwise and streamwise vorticity response to the forcing.

The profiles of the streamwise and the wall-normal velocity magnitude scaled by the amplitude of forcing (A) and the amplification rate predicted by resolvent analysis (σ) are shown in Fig. 4.2 for the 2D forcing cases and in Fig. 4.3 for the 3D forcing cases. The velocity response amplitude extracted from the DNS data is normalized by $\sigma A u_r$ and is expressed as $|u_{r,i}| = C_r |\tilde{U}_i| / \sigma A u_r$ where C_r is a chosen scaling constant (1.22 for 2D forcing and 2.12 for 3D forcing). Note that only the first singular mode is used in the resolvent analysis prediction of the velocity response. The contribution of higher singular modes as well as the changes in the amplification factor, σ , due to changes in the mean velocity profile are the likely reasons for the observed differences in the mode shapes obtained from the DNS and the first resolvent mode. For small forcing amplitude, a good

collapse of the profiles in Figs. 4.2 and 4.3 indicates that the velocity response magnitude scales linearly with the forcing amplitude. However, for large forcing amplitude, the response amplitude scaling is less than linear, consistent with the significant changes in the mean velocity profile observed in Fig. 4.4.

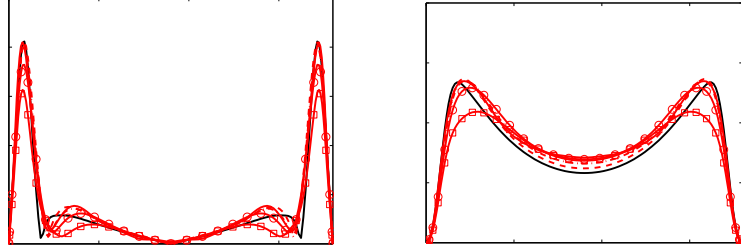


Figure 4.2. Comparison of the shape of the velocity response obtained from DNS (red) and the resolvent analysis (black) is shown for varying values of 2D forcing amplitude. (a) Streamwise and (b) wall-normal responses. Line with squares represent the highest amplitude forcing.

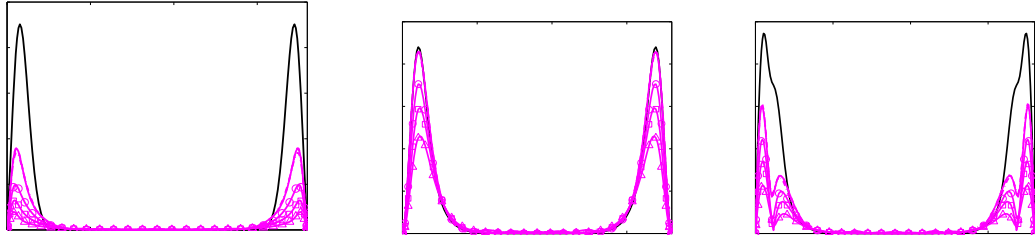


Figure 4.3. Comparison of the shape of the velocity response obtained from DNS (magenta) and the resolvent analysis (black) is shown for varying values of 3D forcing amplitude. (a) Streamwise, (b) wall-normal responses and (c) spanwise responses. Line with triangles represent the highest amplitude forcing.

The profiles of the mean streamwise velocity in plus units are shown in Fig. 4.4 for cases with two- and three-dimensional forcing. It can be observed that the mid-channel mean velocity decreases progressively with increasing forcing amplitude. The changes in the mean velocity are restricted primarily in the region $y+ \geq 14$, above the critical layer, where the mean velocity is $\bar{U} \geq 10$. This is also consistent with the fact that the mean-pressure gradient is kept constant and, therefore, the change in mean wall shear stress should be zero.

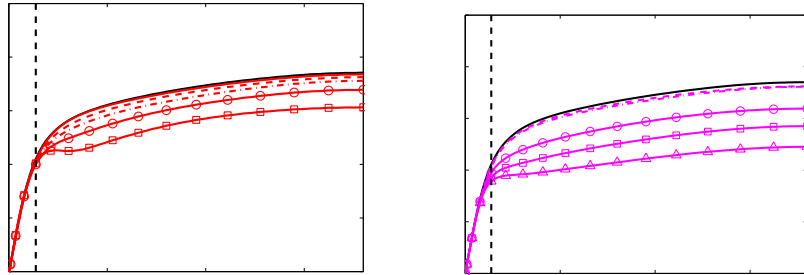


Figure 4.4. The mean velocity profiles for varying forcing amplitudes for 2D (a) cases and 3D (b) cases as a function of $y+$. Black line represents the unforced channel flow. The location of the critical layer is indicated by the dashed line.

The influence of the forcing on the mean velocity is determined by the mean momentum equation. For a fully-developed turbulent channel flow, the equation relates the changes in the mean velocity to the variations in the Reynolds shear stress (Reynolds and Hussain, 1972). The mean Reynolds stress has a wave component ($\langle \tilde{U}_1 \tilde{U}_2 \rangle$) and a turbulent component ($\langle U_1'' U_2'' \rangle$). In the absence of forcing, the contribution of the wave component is zero and the total shear stress is comprised only of the turbulent and viscous component. We find (no figures shown) that for small amplitude of forcing, the total Reynolds shear stress does not vary much from the unforced case. The wave Reynolds shear stress, which scales with the square of the forcing amplitude, is relatively small and the turbulent component is the dominant contributor to the total Reynolds shear stress. For high amplitude forcing, the magnitude of the wave component becomes significant and the turbulent Reynolds shear stress profile undergoes evident changes. For the cases explored, there was a net increase in the total peak shear stress compared to the unforced case. The expected collapse of the sum of the mean viscous stress and Reynolds shear stress to a straight line was observed and suggests that changes in the mean velocity profile for different amplitudes of forcing are constrained by changes in the Reynolds shear stress.

We have examined in detail the changes in the kinetic energy associated with the mean, wave and turbulent components for two- and three- dimensional forcing. The decrease in the mean velocity with increasing forcing amplitude (Fig. 4.4) implies a reduction in the mean component of the kinetic energy. For small amplitude forcing, we find the changes in the overall fluctuation kinetic energy are small. The wave kinetic energy scales with A^2 . At high forcing amplitude, a large increase in the fluctuation energy is evident for the 2D cases. This change is primarily driven by the increase in wave kinetic energy. For the 3D forcing, the peak total fluctuation kinetic energy is observed to decrease slightly with increasing forcing amplitude. This occurs primarily due to a substantial decrease in the peak turbulent kinetic energy that is only partially compensated by an increase in the peak wave kinetic energy.

The decomposition of kinetic energy into the three components (mean, wave and turbulent) and their interactions are depicted in Fig. 4.5. In the right partition of each box, the spectral representation of each component is given. The mean kinetic energy is the energy at zero wavenumber and frequency ($K=0$), whereas energy at the forcing wavenumber and frequency, $K=K_f=(k_x, k_z, \omega)$, represents the wave kinetic energy. The turbulent kinetic energy is the energy at all wavenumbers and frequencies other than $K=0$, K_f . The individual production terms represent the energy transfer between the mean, wave and turbulent components. The energy is input to the mean component through the mean-pressure gradient. The energy is transferred from the mean to the wave and turbulent components through the interaction of mean shear with the wave Reynolds stress and the turbulent Reynolds stress, respectively. The wave component receives support from the external forcing and exchanges energy with the turbulent component through the wave-induced fluctuations in the turbulent Reynolds stress. The mean, wave and turbulent dissipation terms are expressed in terms of the strain rate tensor (S_{ij}) using the mean velocity, the wave response velocity and the turbulent fluctuation velocity, respectively.

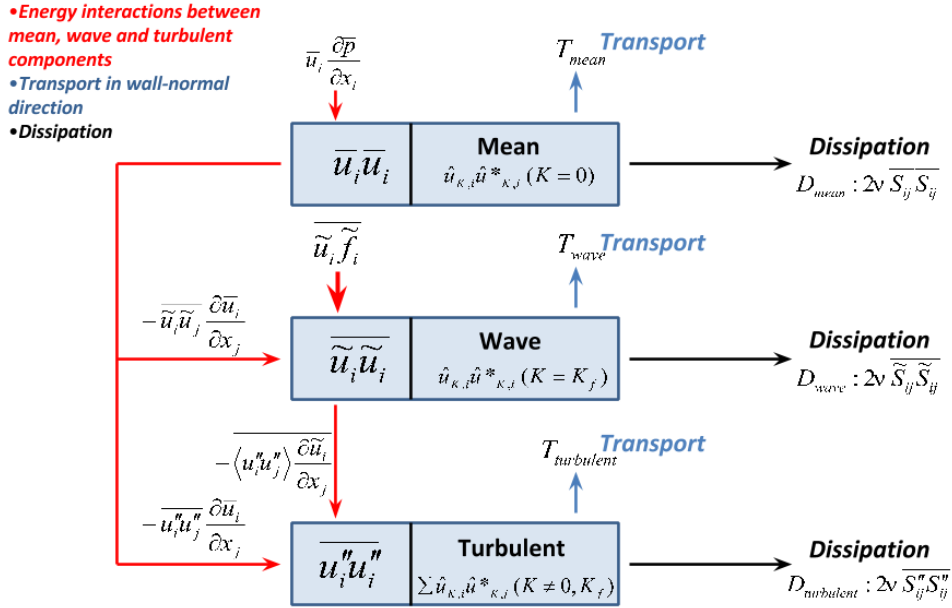


Figure 4.5. Schematic showing the energy interactions between the mean, wave and turbulent components of the mean kinetic energy.

A detailed study of the profiles of the production and dissipation terms for the wave and turbulent kinetic energy equations (not shown) suggested a scaling of external energy input, mean-to-wave energy transfer and the wave energy dissipation with the square of the forcing amplitude for small forcing. The external power input was found to be negligible compared to the power transfer from the mean to the wave component for 3D forcing. But the external power input was the dominant term in the wave energy budget for the 2D forcing cases.

Finally, we considered a scaling of the magnitude of the velocity response (say U) with the forcing amplitude (A). The streamwise, wall-normal and spanwise length scales are λ_x , h and λ_z . For the given forcing speed, c , the forcing time-scale, τ , can be associated with the convection due to wave-speed, $\tau = \tau_{conv} = \lambda_x/c \sim 1/\omega$ (for small-amplitude forcing) or with the acceleration due to the forcing wave, $\tau = \tau_{acc} = (\lambda_x/A)^{1/2}$ (for high-amplitude forcing). Note that for small amplitude forcing ($A \ll c^2/\lambda_x$), the effects of acceleration over the forcing time-period are negligible ($\tau_{acc} \gg \tau_{conv}$).

The mean streamwise velocity and the mean-velocity gradient can be scaled by the convection velocity (U_c) and inverse of the maximum strain-rate, $1/S$, respectively in the equation governing the velocity response. We seek the response due to forcing to be $O(1)$, that is, $A\tau/U \sim 1$. This means that for small amplitude forcing, $U \sim A/\omega$ and for high amplitude forcing, $U \sim (A\lambda_x)^{1/2}$. We do, in fact, find in the wall-normal response a trend towards the $A^{1/2}$ scaling can be observed at large forcing amplitude and A at small amplitude. The magnitude of the response velocity is of the order of wave-speed, that is $U \sim c$, for high-amplitude forcing, $A \sim c^2/\lambda_x$.

In the non-dimensional momentum equation governing the velocity response, the viscous terms are weighted by the inverse of the Reynolds number associated with the wave ($Re_{wave} = \lambda_x c/v \sim c^2/\omega v$ and $\lambda_x^{3/2} A^{1/2}/v$ at small and high forcing amplitude, respectively). This means that at small values of forcing amplitude, the forcing wave essentially sets up a local Stokes' layer close to the wall (analogous to the classical second problem of Stokes'). At high forcing amplitude, the Reynolds stresses associated with the wave become important and give rise to a mean motion. In particular, the wave component of the Reynolds stress is setup such that it results in a decrease in the mass flux. This is similar to the streaming effect that results in the generation of mean flow due to the oscillatory motion of a body (Schlichting and Gersten, 2000). Finally, we find that at low forcing amplitude, $\langle u_i'' u_j'' \rangle$ appears to scale with $O(A^{1/2})$ and $O(1)$ for two- and three-dimensional forcing, respectively. At high forcing amplitude, $\langle u_i'' u_j'' \rangle$ appears to vary as $O(A)$ and $O(A^{1/2})$ for two- and three-dimensional forcing, respectively. This suggests a more effective mixing due to the three-dimensional forcing as opposed to the two-dimensional forcing, even at low forcing amplitude. This later suggestion also corresponds with our finding that applying the 2D waveform forcing but only in regions discretized in the spanwise direction is quite effective while applying it in streamwise discrete regions was not.

5. Capacitive Shear Stress Sensor Development

The capacitive shear stress sensor (CSSS) was developed at the University of Florida, with the objective in this project of characterizing the wall shear stress associated with a synthetic mode introduced using dynamic roughness in the Caltech experimental facilities. In this section, the results concerning sensor development are outlined. The boundary layer results are described in section 6 below.

5.1 Sensor fabrication

Sensor fabrication consisted of a six mask process at the UF Nanoscale Research Facility (NRF) utilizing externally sourced silicon-on-insulator (SOI) wafers with integrated through-silicon-vias (TSVs) provided by IceMOS Technologies. A buried oxide (BOX) of $1.5\mu\text{m}$ separates a Phosphorous doped $50\mu\text{m}$ device layer from the Boron doped $400\mu\text{m}$ handle.

Improper deposition of oxide over TSV contact sites by IceMOS required an additional etch window step before normal processing. Concerns remained over the uniformity and handle isolation at the backside TSVs. Alternating buffered oxide etches (BOE) with sputtered Al/Si (2%) deposition places metallized contact pads on either end of the TSVs. Deposition of a nitride layer on wafer backside acts as passivation. Thermal annealing in forming gas increases contact quality of the pads until TSV connections are confirmed with probe station measurements as Ohmic.

DRIE etching of the frontside defines the floating element structure, and makes trenches separating individual die in the device layer. A second DRIE on the backside opens a large cavity behind the floating element for release of the structure, as well as separating die in the handle layer as well. After BOX etch this allows for individual die selection without use of a dicing saw, improving yield of workable devices.

Release of the floating elements with BOE was incomplete near the tether anchor points. This necessitated a secondary release step using RIE plasma. Selectivity of the RIE between oxide and silicon is roughly 2:1, and thus resulted in over-etching of floating element features. The result of this is reduced sensor resonance due to thinner tethers, and possibly decreased sensitivity from a larger nominal comb finger gap. Further iterations will use a vapor-phase hydrofluoric acid etch for device release with a thicker BOX layer, eliminating the need for a backside cavity etch.

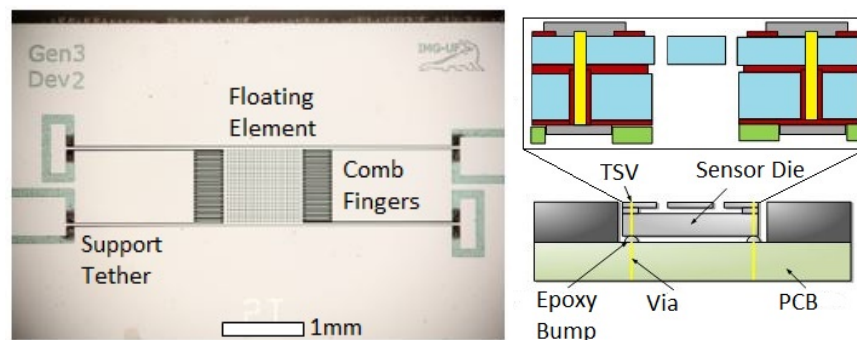


Figure 5.1: (i) Microscope image of fabricated CSSS die. (ii) Schematic of CSSS and sensor cap packing. Yellow posts are TSVs.

Devices with and without TSVs were made from the same fabrication run. Operational device selection was carried out with forced electrostatic actuation with visual confirmation. Cracked and non-working devices were set aside, and operational devices were packaged. Figure 5.1 shows a microscope image of an operational device, and a schematic of initial sensor cap packaging.

5.2 Sensor packaging

Packaging is realized inside a stainless steel tube, with 0.5" outer diameter and 2" of overall length. The sensor die is flip-chip bonded on to a woven Kevlar and aramide epoxy laminate PCB. A layer of film epoxy sits within a recessed pocket on the topside of the PCB, and bonds to the die with a heat curing cycle.

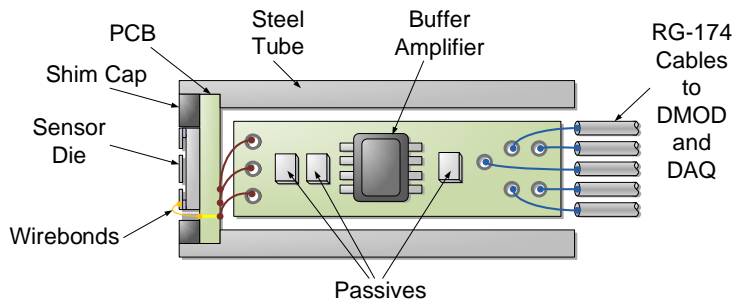


Figure 5.2: Schematic of non-TSV sensor tube packaging.

For non-TSV devices, frontside wirebonds connect the three die electrodes to bond pads on the PCB. A plastic shim cap is laser machined with an Oxford picosecond laser, and affixed around the CSSS die for flushness. Silicone RTV is deposited on top of the exposed wirebonds to encapsulate and protect them from the flow. A schematic of the packaged sensor unit is shown in figure 5.2.

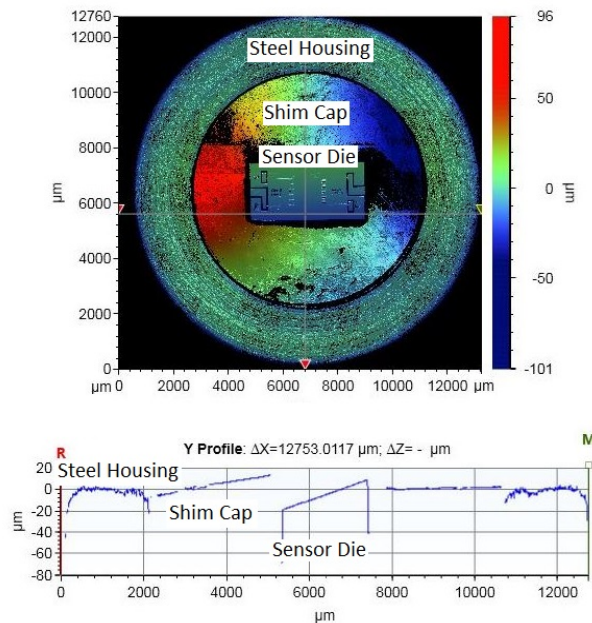


Figure 5.3: SWLI measurement of fully assembled sensor with integrated TSVs. For low flow speeds it can be considered hydraulically smooth.

For TSV devices, an extra slot is milled through the PCB substrate. Wirebonds are connected through the slot from the backside of the die to the backside of the PCB. Silicone RTV is used as wirebond encapsulant again. Scanning white light interferometry (SWLI) measurements of the fully packaged device show maximum deviations of roughly 50-70 μ m. Figure 5.3 shows the SWLI measurement results. This level of roughness is considered hydraulically smooth (<100 μ m) for the low flow speeds investigated.

Solder pads on the backside of the PCB are wired to a unity gain buffer amplifier which is located inside the steel tube. This retains the signal information, while moving from the high output impedance of the silicon die to the low output impedance of the op-amp, improving signal quality received by the interface circuit.

Characterization and testing results reported here were accomplished with non-TSV devices. Final packaging and characterization of devices with TSVs is ongoing.

5.3 Interface circuitry

To simultaneously measure mean and dynamic wall shear stress inputs in real time, a synchronous modulation and demodulation interface circuit (SMOD/DMOD) was developed. Standard DC biasing of electrostatic capacitive transduction sensors only allows for the transmission of AC signal information. The application of sinusoidal biases allows for the measurement of mean capacitance shifts as a change in carrier signal magnitude. A flow chart of different circuit functions is shown in figure 5.4.

Standard AC wall power is shifted to +/-12V and +/-5V rails via a series of regulators. A Colpitts oscillator generates a 1 MHz signal, which is passed through a variable gain amplifier and then split between buffer and inverting amplifiers. The two 180 phase shifted sinusoids are supplied to the differentially positioned comb finger sets. With zero shear stress input, the ideal output from the common sensor electrode is zero. Mean shifts in one direction reduces the static gap between one electrode pair, and increases the other, resulting in an increase of the associated carrier. A mean shift in the opposite direction then results in an increase of the other carrier, allowing for directional information to be obtained. The signal is then buffered inside the packaged sensor head, and sent back to the SMOD/DMOD board.

Band-pass filtering reduces low-frequency noise and high-frequency carrier harmonics, before the signal is split again between buffer and inversion amplifiers. To ensure proper retention of phase during rectification, a timing control block of the circuit generates a phase locked signal. The 50% duty cycle square wave uses the original oscillator output as a trigger, with an adjustable phase block to tune out small offsets. Rectification is then achieved by switching between the buffered and inverted signals. Low-pass filtering of the rectified signal returns the envelope of the carrier signals, which contains both mean and dynamic flow-driven information. DAQ requirements are greatly relaxed, as sampling can be done around the baseband frequency ranges of interest.

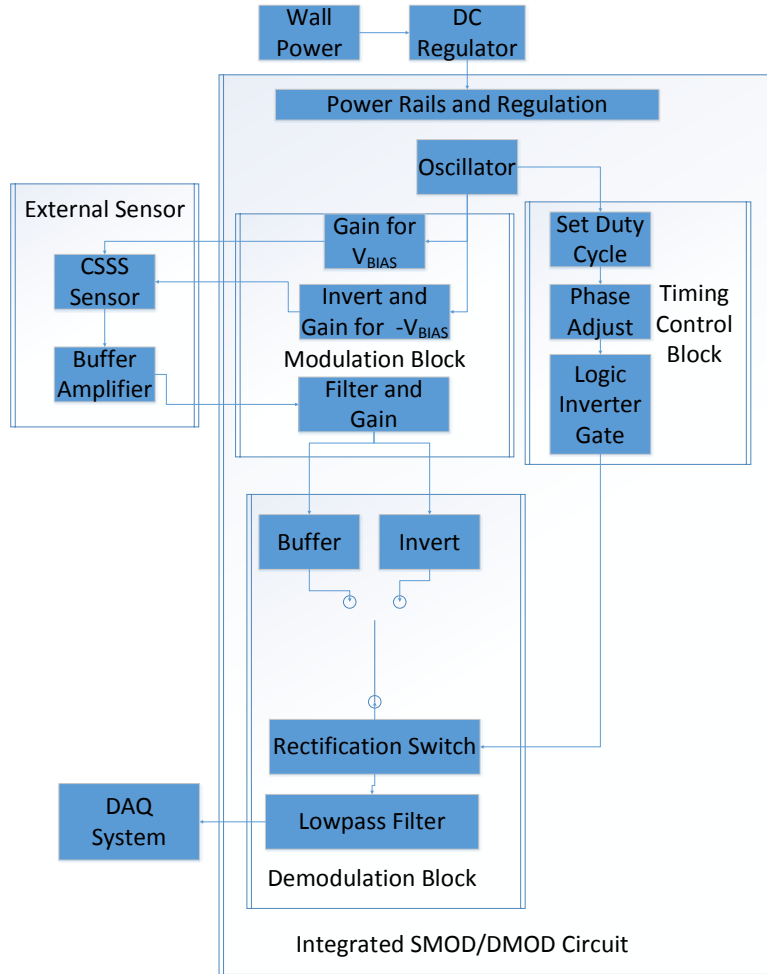


Figure 5.4: Top level flow chart of SMOD/DMOD circuit functionality.

5.4 Characterization

Characterization efforts can be broadly separated into mean and dynamic (DC and AC) components. DC characterization measurements are made with a Keithley 2000 Digital Multi-Meter (DMM) with the CSSS located inside a UF laminar flow cell testing rig.

DC stability is evaluated as variations in system output over time with no forced input. Seen in figure 5.5, this drift is measured as less than 0.2 mV/hour, or less than 0.1 Pa/hour. Sensitivity to mean wall shear stress is evaluated by increasing the input flow rate of the laminar flow cell, with shear stress estimates from pressure differential measurements via equation 1.

$$\tau_w(y = 0) = \frac{h}{2} \frac{dP}{dx}$$

Sensitivity is measured as 3.44 mV/Pa, with data seen in figure 5.6. Bi-directional sensing is confirmed by rotation of the sensor 180 degrees within the flow cell, so the floating element is displaced in the opposite direction. Moving the flow input in a step-wise ramp for both rotational sensor configurations shows the resulting opposing polarity voltage shifts in figure 5.7.

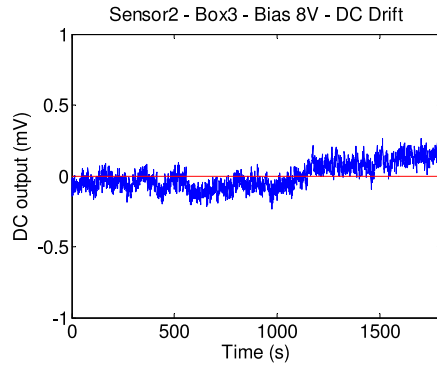


Figure 5.5: DC stability test result. CSSS system output with no flow input over time.

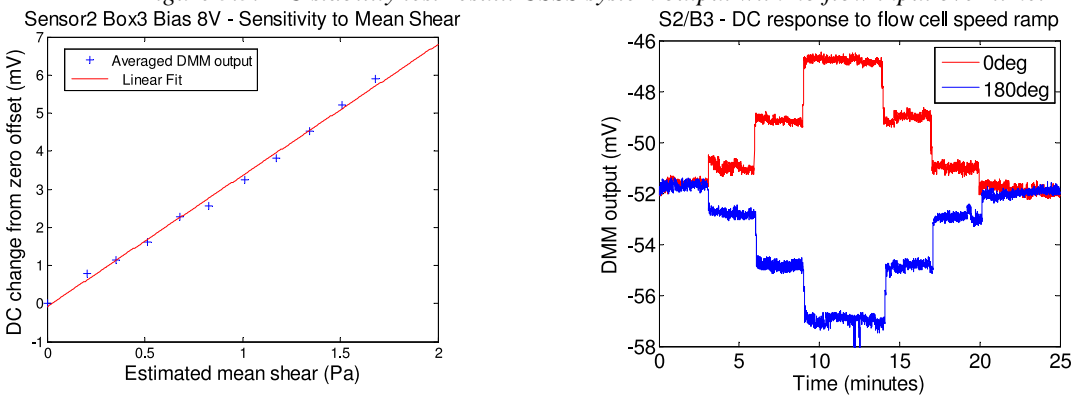


Figure 5.6: Sensitivity of CSSS to mean wall shear stress changes in laminar flow cell.

Figure 5.7: Directionality testing of CSSS in laminar flow cell. The flow speed is ramped in a step-wise fashion in two sequential tests. The sensor is rotated 180 degrees between runs.

As a sensor utilizing an electrostatic transduction method, the CSSS is susceptible to significant changes in the ambient electromagnetic field near the sensor. This can be problematic for wind tunnels with models formed from acrylic. During wind tunnel operation vibrations of the model lead to a buildup of electrical charge on acrylic pieces, due to the triboelectric charging phenomenon. As a relative insulator it is difficult to dissipate this charge with a grounding line, leading to a transient change in the ambient electrostatic field inside the test section, eventually reaching a steady state. This charge buildup results in a change in CSSS DC output, confounding DC measurement results at full scale. The effect is observed in the Caltech Merrill facility, seen in figure 5.8, and also in the UF ELD tunnel of similar design. An effort to quantify the effect was made by covering the sensor and running the tunnel, such that the majority of system response would be from electrostatic changes alone. However this method needs further investigation and calibration to be considered effective. Switching to a grounded aluminum plate insert eliminated the charging effect altogether.

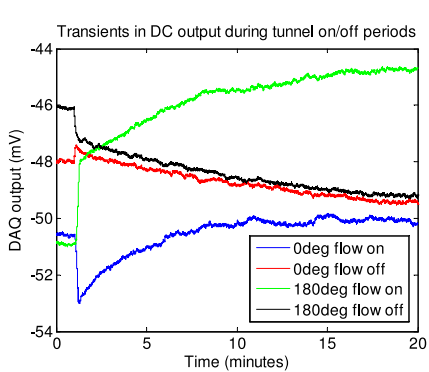


Figure 5.8: CSSS response during tunnel turn on and turn off. The large jump in response is from flow rate changes. The long rolling period is due to electrostatic charging of the acrylic plate model.

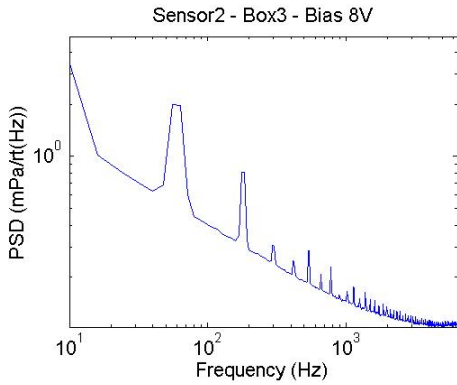


Figure 5.9: Noise floor of CSSS system, in Pa. Sensitivity of 3.45mV/Pa applied across all frequencies.

System noise floor is measured with a SRS750 spectrum analyzer. An 800 FFT line over 10kHz measurement is shown in figure 5.9. Values of 1200 nV/vHz at 100 Hz and 360 nV/vHz at 1000 Hz are measured, corresponding to 340 μ Pa and 120 μ Pa respectively.

An acoustic plane wave tube is used for characterization of dynamic wall shear stress response, utilizing a B&K PULSE system for data acquisition. A compression driver at the PWT entrance drives an oscillating pressure gradient, establishing a standing wave pattern due to the sound hard termination at tube end. Estimates of input wall shear stress are calculated from a solution to the Stoke's oscillating flow solution, defined in equation 2.

$$\tau_w(\omega = 2\pi f_{test}) = -\frac{1}{c} \sqrt{j\omega v} \tanh\left(a \sqrt{\frac{j\omega}{v}}\right) \frac{e^{jkd} - Re^{-jkd}}{e^{jk(d-\delta)} - Re^{-jk(d-\delta)}} P_{measured} e^{j\omega t}$$

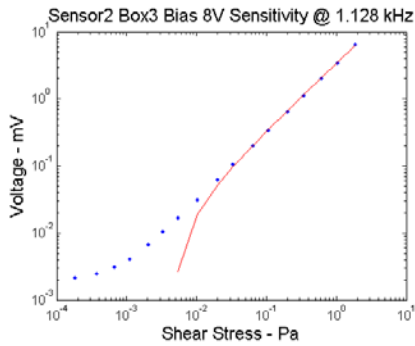


Figure 5.10: Sensitivity calibration of CSSS inside acoustic PWT.

Locating the CSSS at a pressure node allows for isolation of wall shear stress response. The compression driver is supplied higher voltages to increase the pressure perturbations, resulting in the sensitivity curve seen in figure 5.10. Dynamic sensitivity in the linear response region is measured as 3.45 mV/Pa. A frequency response function is generated using the PWT with an adjustable end wall termination, which allows the CSSS to be positioned at a pressure node at any given input frequency. Resonance is identified at 3.5 kHz. Sensitivity to pressure is measured by placing the CSSS into the end wall of the PWT. A pressure sensitivity of 0.98 μ V/Pa is calculated, corresponding to a pressure rejection ratio of 72 dB.

6. Experimental Results

The experimental campaign centered on the use of dynamic roughness to inject one or two synthetic large-scales into an otherwise unperturbed turbulent boundary layer, and the characterization of these synthetic scales using hot-wires and the CSSS. The dynamic roughness technique has been used in the McKeon group over several years, so a brief summary of the operation is given here, along with appropriate references containing further information.

6.1 Experimental set-up

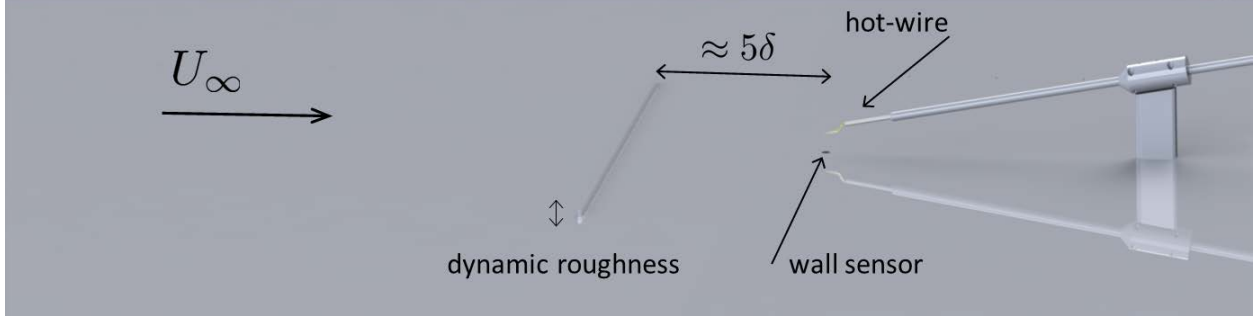


Figure 6.1: Flat plate set-up, showing the locations of the dynamic roughness, the hot-wire and the wall sensor (either the CSSS or a microphone) locations.

The experiments were performed in the Merrill wind tunnel at the California Institute of Technology. The tunnel has an adjustable height ceiling allowing for a nominally zero-pressure-gradient boundary layer to develop over a flat plate. As shown in figure 6.1, the flat plate contains an insert to allow for a thin, spanwise aligned rib to oscillate up and down at a prescribed frequency. At the trough of the oscillation the rib sits flush with the wall and the peak-to-peak amplitude is set by the user. The rib is driven by a linear actuator (Bose, LM1) and its position is recorded with a linear encoder to allow for phase-locked measurements. The dynamic roughness introduces a nominally spanwise-constant disturbance with fixed time-scale(s) and streamwise lengthscales determined by the flow, which can be detected in the downstream sensors.

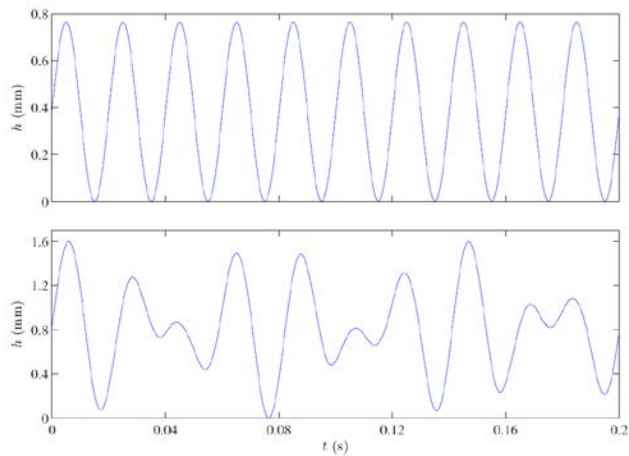


Figure 6.2: Time variation of the dynamic roughness amplitude for (top) 50 Hz single frequency and (bottom) 35 and 50 Hz, two frequency operation, obtained from a linear encoder. $h=0$ corresponds to the unperturbed wall location.

Velocity measurements were made with a Dantec boundary layer hot-wire probe (type 55P05) and pressure measurements were made with a B&K pressure-field microphone (type 4138). The CSSS and the microphone were mounted flush at the wall (not simultaneously) at the same streamwise location as the hot-wire. Full traverses of the hot-wire were performed to record velocity across the thickness of the boundary layer. For these particular set of experiments, the free stream velocity was $U_{\text{infty}} = 22.4$ m/s, yielding a boundary layer thickness of approximately $\delta = 17$ mm and a Reynolds number based on momentum thickness of $Re_\delta \sim 3100$. The roughness frequency and amplitude was 50 Hz and 1 mm respectively, and the corresponding streamwise wavelength of the disturbance was approximately 15 incoming boundary layer thicknesses.

A plane wave tube configuration similar to that described in section 5 above was used to determine the phase relationship between velocity, pressure and wall shear stress. The inlet to the Caltech PWT was modified to allow for mean flow to pass through, which is necessary to avoid hot-wire signal rectification. A preliminary analysis of the PWT calibration data suggests a phase discrepancy between the various sensors no larger than $10-15^\circ$. This estimate will be refined and is the subject of on-going work.

6.2 Characterization of a single synthetic mode

The preliminary characterization of the single frequency (50 Hz) synthetic mode 5δ downstream of the roughness location is shown in figure 6.3. This figure shows the phase-averaged variation of streamwise velocity, wall pressure and wall shear stress over one period of roughness oscillation. Clearly the streamwise velocity signal is coherent over much of the boundary layer thickness, with a reasonably abrupt phase change occurring around $y/\delta = 0.3$. Previous work has shown that the synthetic mode is reasonably well modeled by the resolvent analysis with the appropriate wavenumbers and wavespeed (in the experiments the frequency is fixed and the streamwise wavenumber determined by analysis of the downstream variation of the phase-locked velocity signal). The wall pressure signal appears shifted by approximately a quarter period of the roughness oscillation, while the wall shear stress is nominally in phase with the velocity, as would be expected.

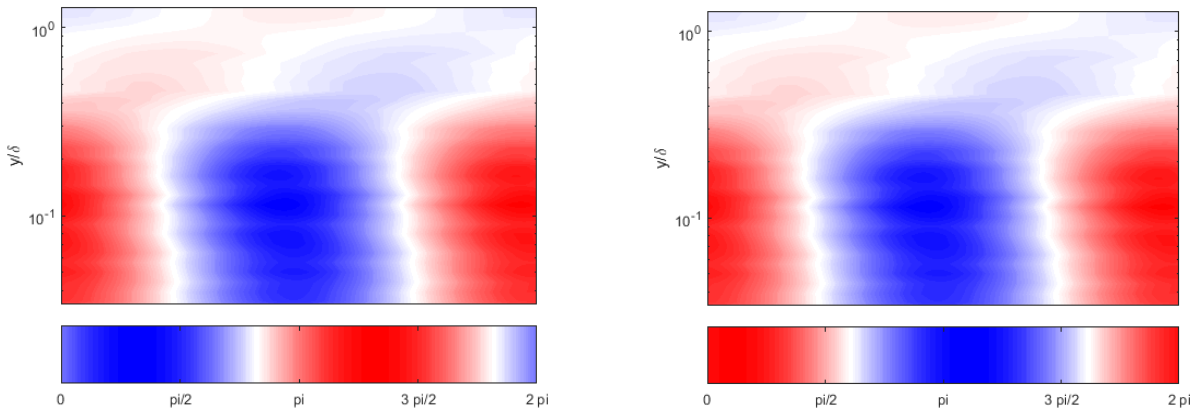


Figure 6.3: Variation of streamwise velocity, pressure and shear stress, obtained from the hot-wire, microphone and CSSS, respectively, over one period of the dynamic roughness actuation ($0-2\pi$ radians). Left: streamwise velocity (top) and pressure (bottom); Right: streamwise velocity (top) and wall shear stress (bottom). Phase accuracy is estimated to be less than 15° . The synthetic mode is characterized by $(k_x\delta, k_z\delta, \omega/(k_x U_{\text{infty}})) = (0.42, 0, 0.5)$.

A direct comparison with resolvent predictions is in progress and will be completed once the relative phase between measurement techniques has been finalized.

6.3 Manipulation of energetic pathways

The pathways of scale interaction and energy transfer were targeted directly by imposing a time-dependent dynamic roughness amplitude containing two frequencies in a distinct experiment. Excitation at 35 and 50 Hz (see figure 6.2 for the amplitude variation) led to the pre-multiplied spectrum shown in figure 6.4, in which both the sum (85 Hz) and difference (15 Hz) frequencies were excited via nonlinear interactions. The table in this figure shows the nomenclature chosen for the two directly excited frequencies (1 and 2) and the two frequencies excited by nonlinear interactions (3 and 4).

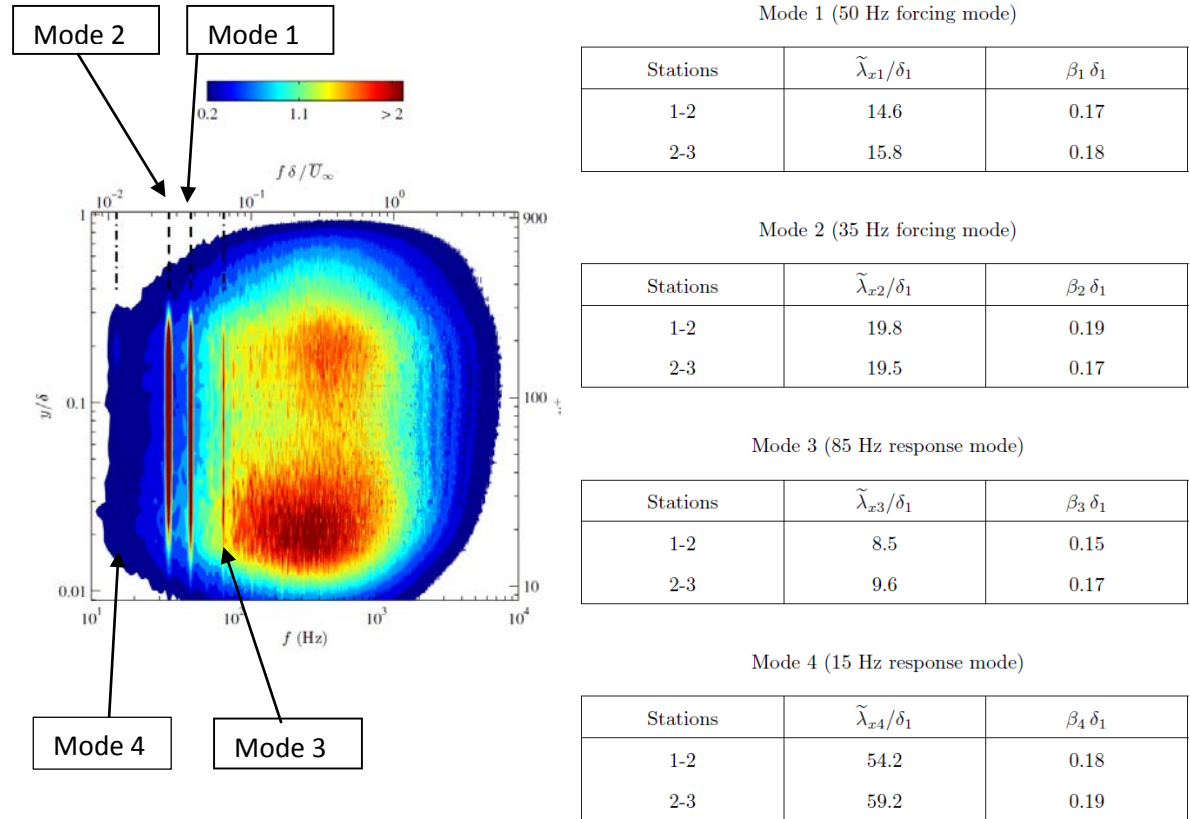


Figure 6.4: (Left) time variation of the dynamic roughness amplitude for (top) 50 Hz single frequency and (bottom) 35 and 50 Hz, two frequency operation, obtained from a linear encoder. $h=0$ corresponds to the unperturbed wall location. (Right) estimated streamwise wavelengths, λ_x , (and decay rates, β) for the directly excited modes (1 and 2) and the sum (3) and difference (4) modes.

Analysis of the phase-locked velocity signals (not shown, but equivalent images to those shown in figure 6.3 for mode 1) reveals that the wavelengths corresponding to modes 3 and 4 are also consistent with the direct nonlinear interaction of modes 1 and 2. We believe this to be the first experimental isolation of individual triadic interactions in wall turbulence.

These results allow direct identification of the details of energy transport in spectral space. As a preliminary characterization of the pathways illuminated by our synthetic mode experiment, a network diagram of the possible interactions between modes 1-4 is shown in the left panel of figure 6.5, where ξ_{ij-k} indicates the interaction between modes i and j giving rise to mode k.

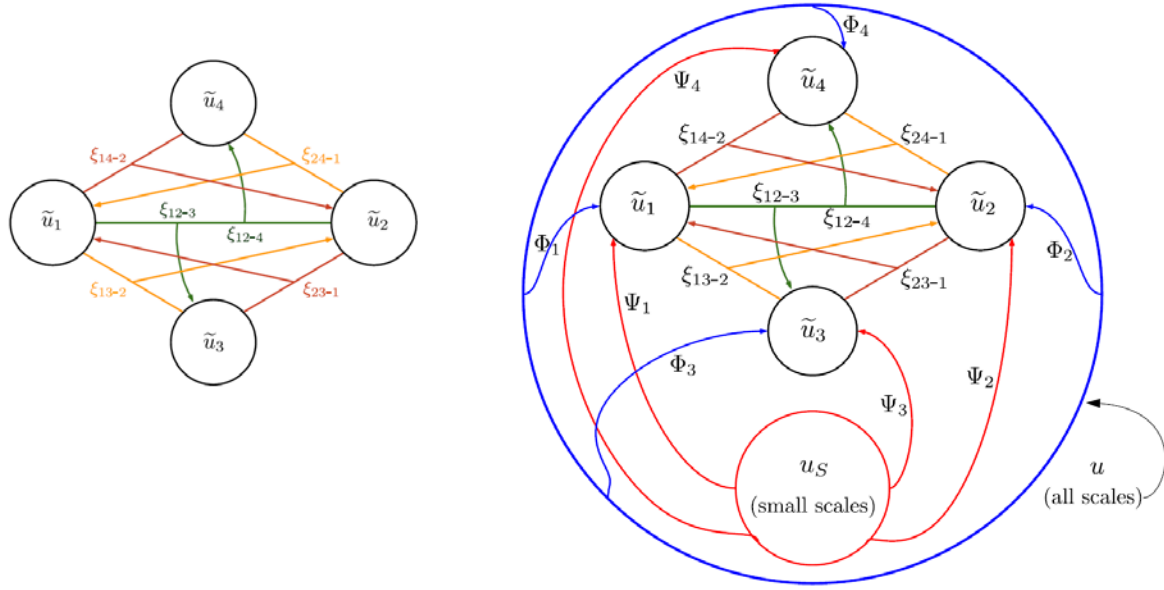


Figure 6.5: Interactions between scales. (Left) direct and indirect interactions associated with the excitation of modes 1 and 2 (see figure 6.4 for mode nomenclature). (Right) interactions related to small scale turbulence activity (u_s) and activity at all energetic scales (u).

Further, turbulence activity at all scales is modified by the presence of modes 1-4 (not shown). The broader picture of the relationship of the synthetic modes 1-4 with all energetic scales in spectral space is outlined in the right panel of figure 6.5. A complete picture of these energy transport pathways is in preparation.

7. Summary and Outlook

During this BRI award, the team has made the following technical contributions to the understanding of wall turbulence:

1. The resolvent framework for analysis of wall turbulence proposed by McKeon & Sharma has been extended to include explicit treatments of pressure fluctuations (rather than imposing a divergence-free basis) and linear time-varying boundary conditions at the wall.
2. The wall boundary condition capability has been exploited to demonstrate that the analysis is capable of capturing important trends concerning the behavior of wall turbulence under opposition control and in the presence of a compliant wall, all without explicitly treating the nonlinear forcing.
3. Fundamental results concerning the characterization of the interaction between turbulent scales have been shown analytically and demonstrated experimentally.
4. DNS results have shown that 3D resolvent-based body forcing couples better to the near wall turbulence than does 2D forcing. The 3D forcing produced greater changes to the mean velocity profile than did the 2D forcing at the same forcing amplitude.
5. The magnitude of the velocity response scales with amplitude scales differently with forcing amplitude depending on whether that forcing amplitude is small or large and a physical mechanism for that difference has been described.
6. 2D traveling wave forcing applied via actuators which are spanwise-discrete may be nearly as effective as 3D forcing.
7. A capacitive shear stress sensor (CSSS) has been developed that is capable of characterizing the wall shear stress, including dynamic fluctuations, in a turbulent boundary layer.
8. Dynamic roughness has been used to introduce synthetic modes into an experimental turbulent boundary layer, leading to changes to the large- and small-scale structure of the turbulence that can be considered to be quasi-deterministic due to the supporting analysis provided under this grant.
9. The CSSS has been used to characterize the single synthetic mode introduced by dynamic roughness into an experimental turbulent boundary layer. This mode resembles a single resolvent (singular response) mode.
10. Energetic pathways between modes have been identified, highlighted and characterized by experimentally exciting two modes and providing the first-known observation of a single triadic interaction.

Resolvent analysis has been shown to be a useful tool for analyzing wall turbulence, both controlled and uncontrolled. Much progress can be made in identifying scales of interest by consideration of the linear resolvent operator

Work to exploit the results summarized above is ongoing and has been the topic of further proposals to AFOSR.

References

Colmenero, G., & Goldstein, D. B. 'Turbulent boundary layer control using wall information' AIAA Paper No. 2004-2116, AIAA Flow Control Meeting, Summer 2004.

*Goldstein, D. B., Handler, R., and Sirovich, L. 'Modeling a no-slip flow boundary with an external force field.' *Journal of Computational Physics*, 105:354–366, 1993.*

*Goldstein, D. B., Handler, R., and Sirovich, L. 'Direct numerical simulation of turbulent flow over a modeled riblet covered surface.' *Journal of Fluid Mechanics*, 302:333–376, 1995.*

*Goldstein, D. B. & Tuan, T-C, 'Secondary Flow Induced by Riblets', *Journal of Fluid Mechanics*, Vol. 363, pp. 115-151 (1998).*

*Halko, N., Martinsson, P.G. & Tropp, J. A. 'Finding structure with randomness: probabilistic algorithms for constructing approximate matrix decompositions' *SIAM Review*, 53(2), 217-288 (2011).*

*Jacobi, I & McKeon, B. J. 'Dynamic roughness-perturbation of a turbulent boundary layer' *J. Fluid Mech.*, 688, 258-296 (2011).*

*Kim, J. 'Physics and control of wall turbulence for drag reduction.' *Philosophical Transaction of the Royal Society of London A*, 369:1396–1411, 2011.*

*McKeon, B. J. & Sharma, A. 'A critical layer framework for turbulent pipe flow' *J. Fluid Mech.*, 658, 336-382 (2010).*

*Meloy, J., Griffin, J., Sells, J., Chandrasekharan, V., Cattafesta, L. & Sheplak, M. "Experimental Verification of a MEMS Based Skin Friction Sensor for Quantitative Wall Shear Stress Measurement", *41st AIAA Fluid Dynamics Conference and Exhibit, AIAA 2011-3995, Hawaii*.*

*Moser, R., D., Kim, J., and Mansour, N. N. 'Direct numerical simulation of turbulent channel flow up to $Re_\tau = 590$.' *Physics of Fluids*, 11:943, 1999.*

*Strand, J., & Goldstein, D., 'DNS of Surface Textures to Constrain the Growth of Turbulent Spots' *J. Fluid Mechanics*, 668, 267-292 (2011).*

*Reynolds, W., C., and Hussain, A. K. M. F. 'The mechanics of an organized wave in turbulent shear flow. Part 3. Theoretical models and comparisons with experiments.' *Journal of Fluid Mechanics*, 54(2):263–288, 1972.*

Schlichting, H. and Gersten, K., Boundary Layer Theory. Springer, 2000.

1.

1. Report Type

Final Report

Primary Contact E-mail

Contact email if there is a problem with the report.

mckeon@caltech.edu

Primary Contact Phone Number

Contact phone number if there is a problem with the report

6263954460

Organization / Institution name

Caltech

Grant/Contract Title

The full title of the funded effort.

Wall turbulence with designer properties:

Identification, characterization & manipulation of energy pathways

Grant/Contract Number

AFOSR assigned control number. It must begin with "FA9550" or "F49620" or "FA2386".

FA9550-12-1-0469

Principal Investigator Name

The full name of the principal investigator on the grant or contract.

Beverley McKeon

Program Manager

The AFOSR Program Manager currently assigned to the award

Ivett Leyva

Reporting Period Start Date

11/15/2012

Reporting Period End Date

11/14/2015

Abstract

The research performed under this BRI award targeted the identification, characterization and manipulation of energy pathways in wall turbulence. The objectives were pursued separately and collaboratively by the California Institute of Technology (Caltech), the University of Florida (UF) and the University of Texas at Austin (UT) teams through a joint numerical, experimental and modeling effort. Our approach applied the team's state-of-the-art capabilities in experiments (Caltech), simulation (UT), MEMS sensor development (UF) and linear algebra techniques (Caltech) to the resolvent formulation of the Navier-Stokes equations for wall turbulence proposed by McKeon & Sharma (2010). This formulation explicitly identifies the pathways for extraction of energy from the mean flow and transfer between wavenumbers, and thus can be used to identify forcing distributions required to manipulate the spectrum. Energetic pathways between modes have been identified, highlighted and characterized by experimentally exciting two modes and providing the first-known observation of a single triadic interaction.

Distribution Statement

This is block 12 on the SF298 form.

Distribution A - Approved for Public Release

DISTRIBUTION A: Distribution approved for public release.

Explanation for Distribution Statement

If this is not approved for public release, please provide a short explanation. E.g., contains proprietary information.

SF298 Form

Please attach your **SF298** form. A blank SF298 can be found [here](#). Please do not password protect or secure the PDF. The maximum file size for an SF298 is 50MB.

[SF-298-McKeon.pdf](#)

Upload the Report Document. File must be a PDF. Please do not password protect or secure the PDF . The maximum file size for the Report Document is 50MB.

[AFOSR-BRI_finalreport.pdf](#)

Upload a Report Document, if any. The maximum file size for the Report Document is 50MB.

Archival Publications (published) during reporting period:

1. Moarref, R., Sharma, A. S., Tropp, J. A. & McKeon, B. J. 'Model-based scaling and prediction of the streamwise energy intensity in high-Reynolds number turbulent channels' *J. Fluid Mech.* 734, 275-316; also ArXiV1302.1594, 2013.
2. Luhar, M., Sharma, A. S. & McKeon, B. J. 'On the structure and origin of pressure fluctuations in wall turbulence: predictions based on the resolvent analysis' *J. Fluid Mech.*, 751, 38-70 (2014).
3. Luhar, M., Sharma, A. S. & McKeon, B. J. 'Opposition control within the resolvent analysis framework' *J. Fluid Mech.*, 749, 597-626 (2014).
4. Moarref, R., Jovanovic, M. R., Tropp, J. A., Sharma, A. S. & McKeon, B. J. 'A low-order decomposition of turbulent channel flow via resolvent analysis and convex optimization' *Phys. Fluids*, 26, 051701 (2014); also ArXiV 1401.6417, 2014.
5. Duvvuri, S. & McKeon, B. J. 'Triadic scale interactions in a turbulent boundary layer' *J. Fluid Mech.*, 767, R4 (2015).
6. Luhar, M., Sharma, A. S. & McKeon, B. J. 'A framework for studying the effect of compliant surfaces on wall turbulence' *J. Fluid Mech.*, 768, 415-441 (2015); also arXiv 1411.6690.
7. Sharma, A. S., Moarref, R., McKeon, B. J., Park, J. S., Graham, M. & Willis, A. P. 'Low-dimensional representations of exact coherent states of the Navier-Stokes equations' (To appear, *Phys. Rev. E.*)

Changes in research objectives (if any):

None

Change in AFOSR Program Manager, if any:

From Douglas Smith to Ivett Leyva.

Extensions granted or milestones slipped, if any:

None

AFOSR LRIR Number**LRIR Title****Reporting Period****Laboratory Task Manager****Program Officer****Research Objectives****Technical Summary****Funding Summary by Cost Category (by FY, \$K)**

	Starting FY	FY+1	FY+2
Salary			
Equipment/Facilities			
Supplies			
Total			

Report Document

Report Document - Text Analysis

Report Document - Text Analysis

Appendix Documents

2. Thank You

E-mail user

Feb 10, 2016 16:10:58 Success: Email Sent to: mckeon@caltech.edu